The Astrophysical Journal, 715:39–50, 2010 May 20 doi:10.1088/0004-637X/715/1/39


# FORMATION AND EVOLUTION OF CORONAL HOLES FOLLOWING THE EMERGENCE OF ACTIVE REGIONS

Y.-M. Wang, E. Robbrecht[1], A. P. Rouillard[1], N. R. Sheeley, Jr., and A. F. R. Thernisien[2]
Space Science Division, Naval Research Laboratory, Washington, DC 20375-5352, USA; yi.wang@nrl.navy.mil, eva.robbrecht@oma.be, alexisrouillard@yahoo.co.uk, neil.sheeley@nrl.navy.mil, arnaud.thernisien@nrl.navy.mil
*Received 2010 February 17; accepted 2010 March 25; published 2010 April 23*

## ABSTRACT

The low level of solar activity over the past four years has provided unusually favorable conditions for tracking the formation and evolution of individual coronal holes and their wind streams. Employing extreme-ultraviolet images recorded with the *Solar Terrestrial Relations Observatory* during 2007–2009, we analyze three cases in which small coronal holes first appear at the edges of newly emerged active regions and then expand via flux transport processes, eventually becoming attached to the polar holes. The holes form gradually over timescales comparable to or greater than that for the active regions to emerge, without any obvious association with coronal mass ejections. The evolving hole areas coincide approximately with the footpoints of open field lines derived from potential-field source-surface extrapolations of the photospheric field. One of these coronal-hole systems, centered at the equator and maintained by a succession of old-cycle active regions emerging in the same longitude range, persists in one form or another for up to two years. The other two holes, located at midlatitudes and originating from new-cycle active regions, become strongly sheared and decay away after a few rotations. The hole boundaries and the small active-region holes, both of which are sources of slow wind, are observed to undergo continual short-term ($\lesssim$1 day) fluctuations on spatial scales comparable to that of the supergranulation. From in situ measurements, we identify a number of plasma sheets associated with pseudostreamers separating holes of the same polarity.

*Key words:* solar wind – Sun: activity – Sun: corona – Sun: heliosphere – Sun: magnetic topology – Sun: surface magnetism

## 1. INTRODUCTION

The Sun's large-scale magnetic field, including its open flux, originates in active regions but is redistributed over the solar surface by transport processes. The open flux is rooted in areas dominated by a single polarity, where the field lines extend to great heights and are dragged out into the heliosphere as the plasma pressure overcomes the restraining magnetic tension, giving rise to coronal holes, solar wind streams, and the interplanetary magnetic field (IMF). (For recent reviews on coronal holes and the solar wind, see Cranmer 2009; McComas et al. 2007; Wang 2009; Zurbuchen 2007.) In extreme-ultraviolet (EUV) and X-ray images, the holes first appear near the outer edges of newly emerged active regions, as very small, dark areas which may be partially obscured by the surrounding diffuse emission (see, e.g., Švestka et al. 1977; Harvey & Hudson 2000; Schrijver & DeRosa 2003; Liewer et al. 2004). As the active-region flux spreads under the influence of supergranular convection and differential rotation, forming larger unipolar regions, the holes increase in size while their footpoint field strengths decrease. The nonaxisymmetric component of the large-scale field is progressively annihilated through the combined action of rotational shearing and supergranular diffusion, and the remnant trailing-polarity flux is carried to the poles and concentrated there by the $\sim$10–20 m s$^{-1}$ surface meridional flow. The cumulative effect of this poleward transport of active-region flux over the sunspot cycle is to establish sharply peaked polar fields and axisymmetric polar holes extending down to latitude 60° in each hemisphere.

The last years of solar cycle 23 have provided unusually favorable conditions for studying the formation and evolution of coronal holes. During the extended period of low activity that followed the launch of the *Solar Terrestrial Relations Observatory* (*STEREO*) in 2006 October, many holes were observed at low and middle latitudes, some of which gave rise to long-lived, recurrent wind streams (see, e.g., Gibson et al. 2009; Lee et al. 2009; Luhmann et al. 2009; Abramenko et al. 2010). Several of these holes can be tracked from their initial appearance in new active regions to their eventual dissolution, and the plasma and compositional properties of their wind streams can be identified at 1 AU.

Here, we focus on three examples in which coronal holes formed following the emergence of active regions and evolved in a manner consistent with surface flux transport. To identify the holes and their changing boundaries, we employ observations from the Extreme Ultraviolet Imager (EUVI) on the *STEREO* A and B spacecraft, which are positioned "ahead" and "behind" the Earth on its orbital path and are separating from each other in heliographic longitude at a rate of 45° yr$^{-1}$ (see Howard et al. 2008). The observed holes are compared with open field regions inferred from a potential-field source-surface (PFSS) extrapolation of the photospheric field, with the source surface (beyond which the field lines are taken to be radial) located at heliocentric distance $r = R_{ss} = 2.5\ R_\odot$. As in Wang et al. (2009b), we average together Carrington maps of the photospheric field from the Mount Wilson Observatory (MWO) and the Wilcox Solar Observatory (WSO). The magnetograph data are corrected for the saturation of the Fe I 525.0 nm line profile by multiplying by 4.5–2.5 $\sin^2 L$, where $L$ denotes heliographic latitude (see Wang & Sheeley 1995; Arge et al. 2002; Ulrich et al. 2002, 2009), and the line-of-sight measurements are deprojected by assuming the photospheric field to be radially oriented at the depth where it is measured.

The plasma and composition properties of the solar wind emanating from the coronal holes are derived mainly from

[1] Also at George Mason University, Fairfax, VA 22030, USA.
[2] Also at Universities Space Research Association, Columbia, MD 21044, USA.

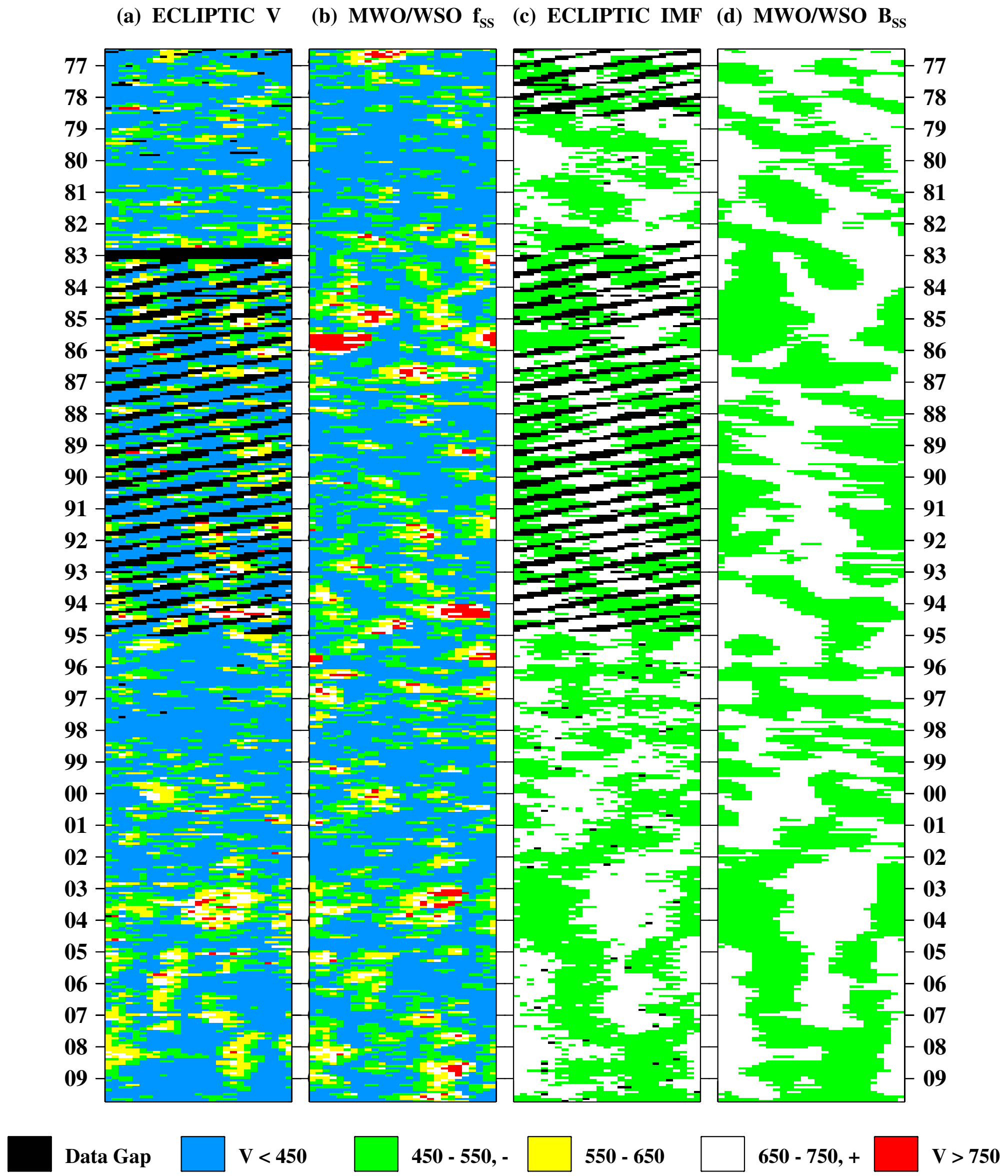


**Figure 1.** Bartels-format (27 day) stackplots showing (a) the daily wind speeds $v$ measured near Earth during 1976–2009 (NSSDC OMNI 2 data), (b) the flux-tube expansion factors $f_{ss}$ or predicted wind speeds $v$ derived from the averaged MWO and WSO photospheric fields, (c) the observed IMF sector polarities at Earth (NSSDC OMNI 2), and (d) the polarities predicted by applying a PFSS extrapolation to the averaged MWO and WSO photospheric fields. Blue: $v < 450$ km s$^{-1}$ ($f_{ss} > 20$); green: $v = 450$–$550$ km s$^{-1}$ ($10 < f_{ss} < 20$); yellow: $v = 550$–$650$ km s$^{-1}$ ($7 < f_{ss} < 10$); white: $v = 650$–$750$ km s$^{-1}$ ($4.5 < f_{ss} < 7$); red: $v > 750$ km s$^{-1}$ ($f_{ss} < 4.5$). In the polarity plots, green (white) denotes inward- (outward-) pointing IMF. Black pixels represent data gaps.

measurements by the *Advanced Composition Explorer* (*ACE*), stationed at the L1 point approximately midway between *STEREO* A and B. These in situ data include (1) hourly averages of the proton bulk speed $v$ and number density $n_p$ from the Solar Wind Electron, Proton, and Alpha Monitor (McComas et al. 1998); (2) hourly averages of the IMF components from the Magnetic Field Experiment (Smith et al. 1998); and (3) two-hour averages of element ratios from the Solar Wind Ion Composition Spectrometer (Gloeckler et al. 1998). The first two data sets are also available from the National Space Science Data Center (NSSDC) OMNIWeb site.

Previous studies have shown that the solar wind speed at 1 AU is inversely correlated with the rate at which the associated flux tube diverges near the Sun, as measured by the parameter $f_{ss} = (R_\odot/R_{ss})^2(B_0/B_{ss})$, where $B_0$ and $B_{ss}$ are the field strengths at the base of the flux tube and at the source surface, respectively (Levine et al. 1977; Wang & Sheeley 1990; Arge & Pizzo 2000).

To place the present epoch in the context of past solar cycles and to illustrate the application of the PFSS and expansion-factor models, Figure 1 shows the evolution of the solar wind speed and IMF sector polarity observed near Earth during 1976–2009 (NSSDC OMNI 2 data), alongside the evolution predicted by extrapolating MWO and WSO photospheric field maps for Carrington rotations (CRs) 1642–2088. Here, daily averages of wind speed and IMF polarity are plotted in 27 day rows (Bartels format). Given the simplicity of the models, the agreement between the predicted and observed patterns is surprisingly good. The recurrent high-speed streams are seen to be more prominent and longer-lived during the declining phase of cycle 23 (∼2003–2009) than during the corresponding phase of cycle 21 (∼1982–1986) and cycle 22 (∼1992–1996). This difference can be largely attributed to the weakness of the polar fields during the present cycle, which delayed the flattening of the heliospheric current sheet toward the ecliptic and maintained the vertical (27 day) patterns seen in the IMF polarity after 2002. With sunspot activity falling to very low levels during the current minimum, horizontal structure becomes clearly evident in the IMF stackplots in early 2008 and early 2009, when the south polar axis is tilted toward Earth and the IMF polarity at the spacecraft is predominantly positive, as well as in late 2009, when negative-polarity flux from the boundary of the north polar hole predominates (see Rosenberg & Coleman 1969).

The expansion factor model predicts that the bulk of the slow solar wind (defined here as having $v \lesssim 450$ km s$^{-1}$) originates from rapidly diverging open field lines rooted in small coronal holes or just inside the boundaries of larger ones (including the polar holes). As discussed in Wang et al. (2009a), some of the well-known compositional differences between high- and low-speed wind (see, e.g., Geiss et al. 1995) can be attributed to differences in the location of the coronal heating; because of the rapid falloff of the field strength in the open field sources of low-speed wind, the energy deposition and temperature maximum occur close to the coronal base, resulting in higher oxygen freezing-in temperatures and the increased evaporation of easily ionized elements from the chromosphere. Additional contributions to the slow wind come from streamer blobs and the heliospheric plasma sheet, both of which have their origin in closed field regions. *STEREO*/SECCHI observations show the blobs to be small flux ropes formed as helmet-streamer loops are stretched outward and pinch off by reconnecting with each other (see Sheeley et al. 2009; Rouillard et al. 2009; Chen et al. 2009; Song et al. 2009). The plasma sheet extensions of helmet streamers (which separate coronal holes of opposite polarity) and "pseudostreamers" (which separate holes of the same polarity) consist of fine raylike structures, which may be formed by continual footpoint exchanges between the streamer loops and the adjacent open field lines (Wang et al. 1998, 2007; Crooker et al. 2004).

## 2. FORMATION OF LONG-LIVED EQUATORIAL HOLES IN 2007

Again referring to Figure 1, we see that the IMF polarity in the ecliptic changes from a four-sector to a two-sector structure in mid-2007. A new high-speed stream then forms within the merged negative-polarity sector and persists until the beginning of 2009. This change coincides with the emergence of an active-region complex just below the equator in 2007 June (CR 2057), which leads to a strengthening of the Sun's equatorial dipole component ($l = 1$, $|m| = 1$) relative to the quadrupole ($l = 2$, $|m| = 2$).

In general, the emergence of an active region may cause the Sun's total open flux to increase, decrease, or remain unchanged, depending on whether the bipole acts to strengthen or weaken the lowest-order multipoles of the photospheric field. In the present case, the equatorial dipole component of the activity complex and that of the background field happen to be longitudinally in phase with each other, resulting in a significant increase in the net dipole strength and the total open flux (see Wang & Sheeley 2003a). In the framework of the PFSS model, the emerging, outward-expanding active-region loops are converted into pairs of opposite-polarity open field lines at the source-surface neutral line (corresponding to the cusps of helmet streamers); the footpoint areas of these loops appear as small coronal holes at the peripheries of the active regions.

Figure 2 shows the rotation-to-rotation evolution of coronal holes during CR 2056–2061 (2007 April 27 through October 8). At the left, we display a sequence of Carrington-format maps constructed from Fe XII 19.5 nm observations recorded with EUVI A. Here, strips of central meridian data were extracted from full-disk images and arranged in a time-reversed sequence; note that a given Carrington longitude $\phi$ is observed at a later (earlier) time from *STEREO* A (B) than it is from Earth. Correspondingly, the maps at the right show the averaged MWO and WSO photospheric fields, with the open field regions derived from a PFSS extrapolation overplotted as dots, color-coded according to the associated value of $f_{ss}$; the colored diamonds (with white lines connecting them to the source regions) indicate the predicted wind speeds in the ecliptic plane.

The main body of the active-region complex emerges around Carrington longitude 180° during CR 2057. As indicated by the arrow in the 19.5 nm map, a low-contrast, negative-polarity coronal hole first appears on the north side of the activity complex. This hole is no longer visible during CR 2058, presumably having closed down due to the emergence of positive-polarity flux on its western side; instead, a dark hole is now present within the negative-polarity region at the far west end of the activity complex. During subsequent rotations, the negative-polarity hole expands in the longitudinal direction, and by CR 2061 it begins to become linked in the latitudinal direction to the north polar hole. Meanwhile, a corresponding (but larger and broader) extension of the south polar hole forms within the positive-polarity region at the eastern end of the activity complex. In this case, a low-latitude hole was already present near $\phi = 110°$ when new bipoles emerged in its vicinity during CR 2057. During CR 2058 and 2059, an extremely narrow, vertically oriented dark lane (arrowed) appears farther to the west, linking the activity complex to the south polar hole. By CR 2061, the positive-polarity hole fragments have merged into a large polar-hole lobe, and the final result is the creation of a pair of opposite-polarity equatorward extensions centered on the decaying activity complex. During this transition from a four-sector to a two-sector polarity structure, the positive-polarity hole that was initially present at $\phi \sim 280°$ becomes progressively sheared and eventually disappears. Comparing the left- and right-hand panels of Figure 2, we find reasonably good agreement between the observed and predicted coronal-hole configurations; in particular, the PFSS model reproduces the narrow lane that forms during CR 2058–2059 at the western edge of the developing south polar-hole extension.

Figure 3 shows the wind speeds, proton densities, Fe/O ratios, and spiral angles measured at the L1 point during CR 2056–2061. Here, the data have been mapped back to the source surface assuming a propagation time of five days (corresponding to a wind speed of ~350 km s$^{-1}$) and are plotted as a function of Carrington longitude, so that time runs from right to left. The spiral angle is measured counterclockwise from the Sun–Earth line and lies in the quadrant 90°–180° (270°–360°) if the field line points away from (toward) the Sun. With the help of this polarity information, the sources of each of the observed wind streams may be readily identified by comparing Figures 2 and 3. The negative-polarity hole that forms along the northwest side of the new activity complex gives rise to the high-speed stream whose location is indicated by the vertical dashes in Figure 3 (left panels). This stream shifts progressively to the west in the 27.3 day Carrington frame, because the active regions from which the hole forms are clustered around the equator and rotate at close to the 26.9 day equatorial rate. The wind stream from the broad south polar-hole lobe develops a twin-peaked structure

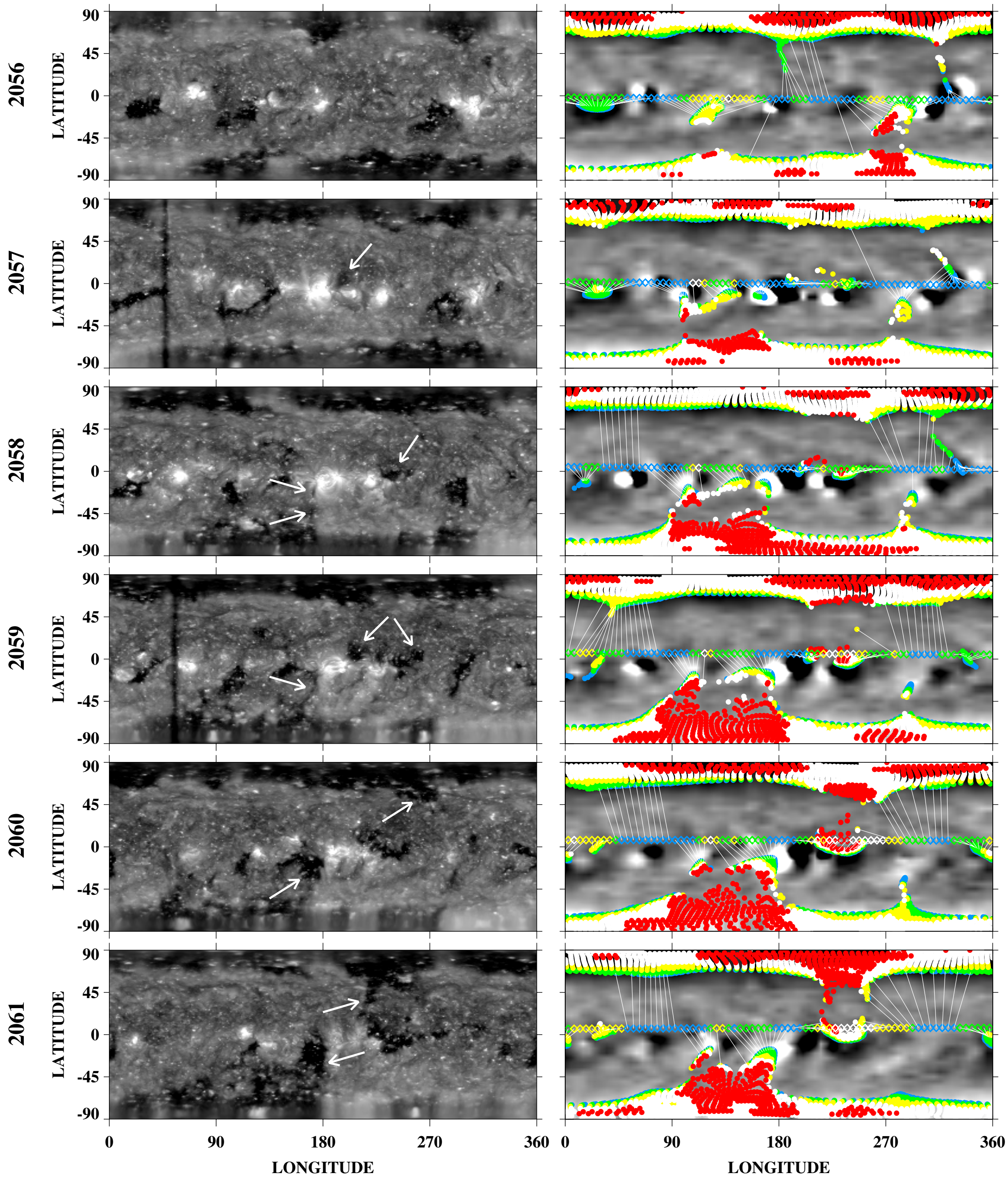


**Figure 2.** Formation of a pair of large equatorial holes following the emergence of an activity complex. Left: sequence of Carrington-format maps showing the distribution of Fe XII 19.5 nm emission observed from EUVI A during CR 2056–2061 (2007 April 27 through October 8). The maps were assembled from the central meridian portions of full-disk images (note that a given Carrington longitude reaches central meridian at a later time as seen from *STEREO* A than as seen from Earth). White arrows point to newly formed coronal holes. Right: corresponding sequence of maps showing the open field regions derived from a PFSS extrapolation, overplotted on the averaged MWO and WSO photospheric field. Colored dots represent the footpoints of open field lines and are coded according to the associated expansion factors and asymptotic wind speeds as in Figure 1. In addition, colored diamonds indicate the predicted wind speeds in the ecliptic plane, with white lines pointing to the corresponding source regions. Grayscale for the photospheric field ranges from $B_r < -10$ G (black) to $B_r > +10$ G (white).

due to the presence of negative-polarity flux at the equator, which splits the low-latitude end of the positive-polarity lobe into two components separated by a pseudostreamer. During CR 2059, a narrow density spike (at $\phi = 120°$, marked "PS") can be seen at the interface between the two positive-polarity streams; we interpret this feature as a remnant of the plasma sheet observed in white-light coronagraph images of pseudostreamers (see Wang et al. 2007). Another pseudostreamer plasma sheet may be seen at $\phi = 266°$ during CR 2060; the corresponding maps in Figure 2 suggest that this density spike occurs at the interface between the negative-polarity hole on the northwest edge of the activity complex and the developing lobe of the north polar hole. Plasma sheets between wind streams of the same polarity have previously been identified by Neugebauer et al. (2002) using *ACE* observations taken at sunspot maximum (see especially their Figures 11 and 13).

The Fe/O ratio, plotted as dots in the left-hand panels of Figure 3, is often taken as a measure of the first-ionization

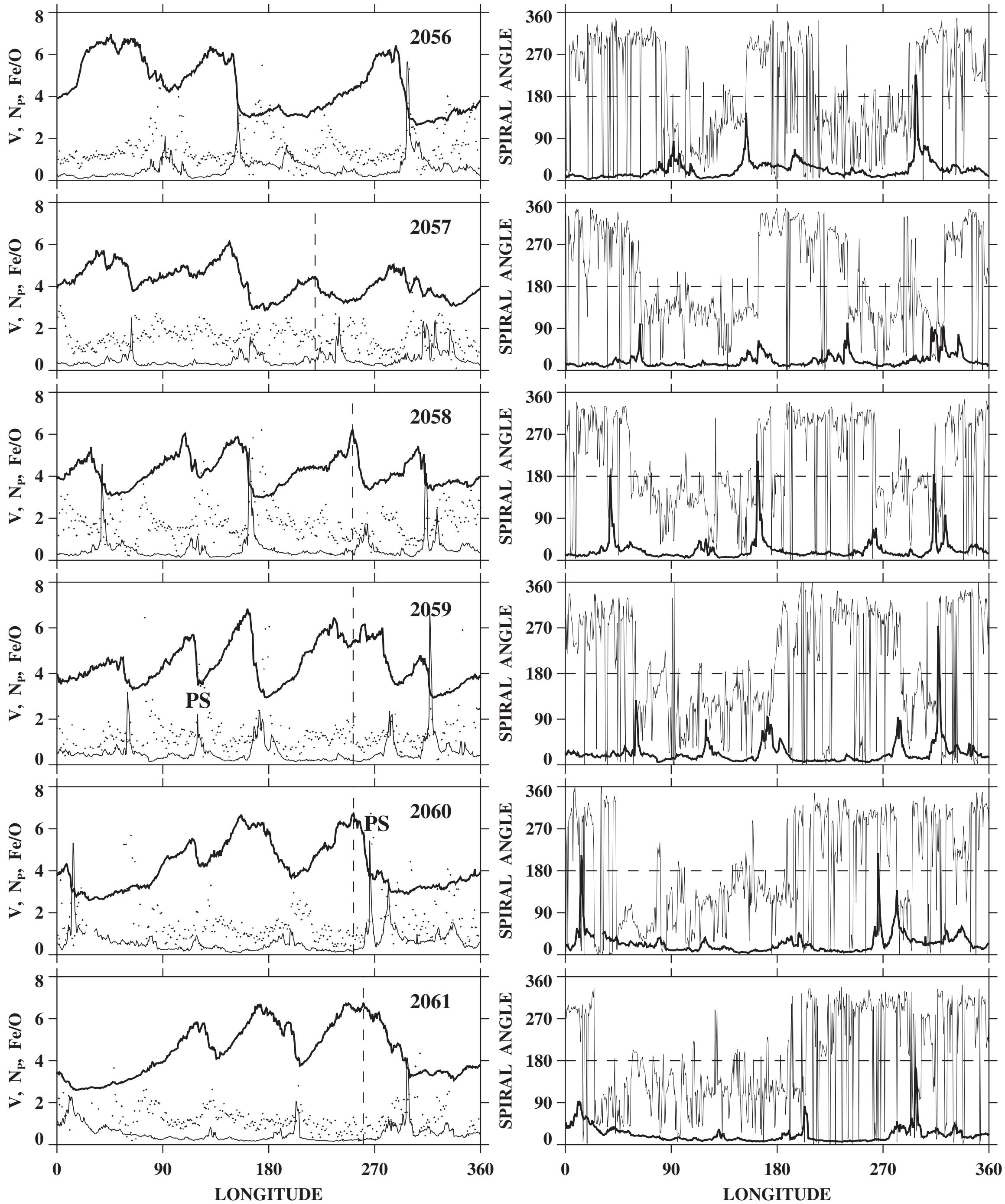


**Figure 3.** Solar wind measurements by *ACE* during CR 2056–2061, plotted as a function of Carrington longitude (so that time runs from right to left in each panel, as in Figure 2). Left: variation of the hourly averaged wind speed $v$ in units of 100 km s$^{-1}$ (thick solid line), hourly averaged proton density $n_p$ in units of 10 cm$^{-3}$ (thin solid line), and two-hour averages of the element abundance ratio $(n_{\rm Fe}/n_{\rm O}) \times 25$ (dotted). Vertical dashes mark the wind stream generated by the negative-polarity coronal hole that forms along the northwestern edge of the activity complex in Figure 2. Density enhancements that may represent pseudostreamer plasma sheets are labeled "PS." Right: variation of the spiral angle (degrees), measured counterclockwise from the Sun–Earth line and lying in the quadrant 90°–180° (270°–360°) if the field line points away from (toward) the Sun. Also plotted is $n_p$ in arbitrary units (thick solid line). All of the measurements have been mapped back to the source surface (so as to be in phase with the Carrington maps of Figure 2), assuming a five-day Sun–Earth propagation time.

potential (FIP) effect in the solar wind, with iron being a characteristic low-FIP element. As found in earlier studies (Geiss et al. 1995; von Steiger et al. 2000; Suess et al. 2009; Wang et al. 2009a), it is apparent that the Fe/O ratio tends to be inversely correlated with wind speed, but with the values showing a large amount of scatter in low-speed wind. Figure 3 also suggests that very strong enhancements in Fe/O often occur around plasma sheets, both those associated with IMF sector boundaries and those without polarity reversals (pseudostreamer plasma sheets).

## 3. FORMATION AND SHEARING OF A MID-LATITUDE CORONAL HOLE

Figure 4 shows the evolution of a coronal hole associated with a new-cycle active region. The small bipolar magnetic region

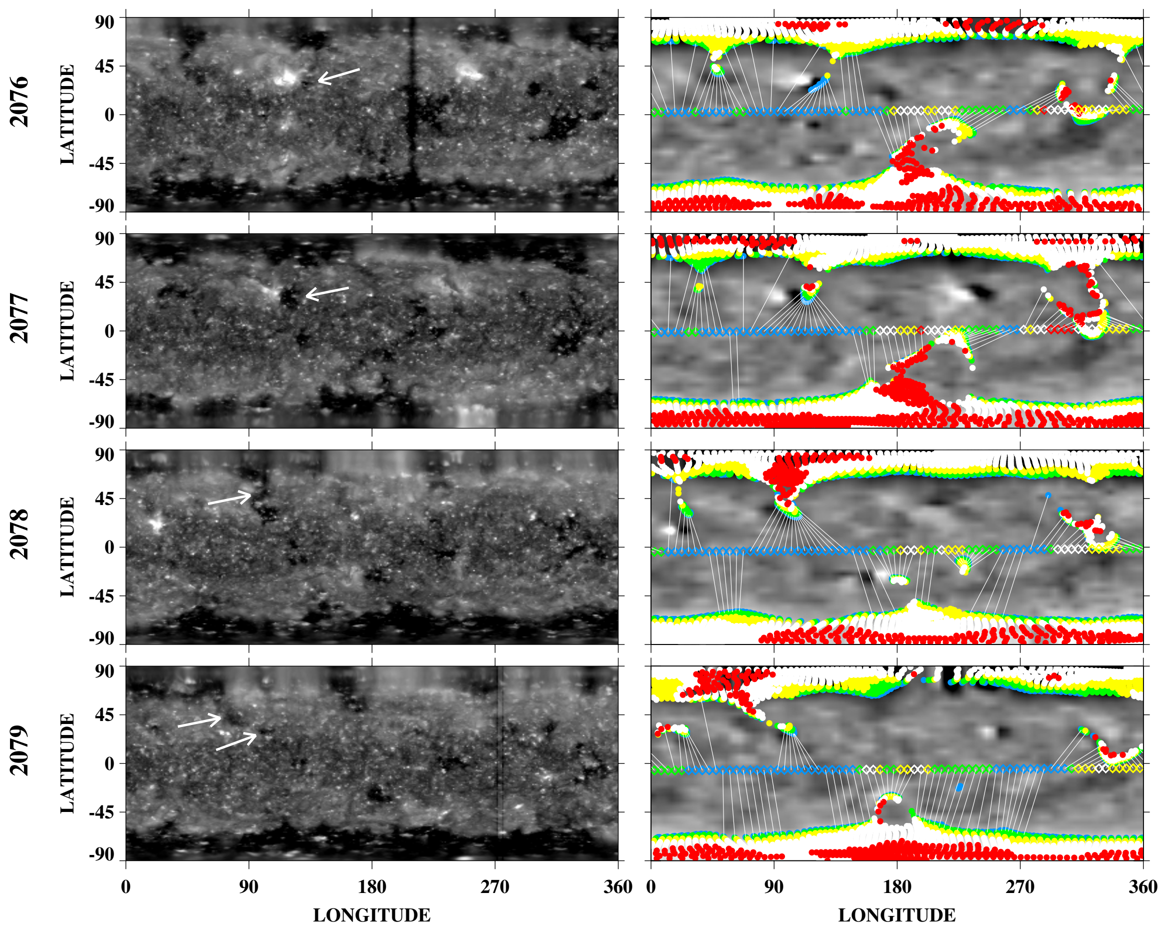


**Figure 4.** Formation and decay of a mid-latitude hole following the emergence of a new-cycle active region. Left: Carrington maps showing the distribution of Fe XII 19.5 nm emission during CR 2076–2079 (2008 October 23 through 2009 February 10). The observations for CR 2077 are from EUVI B, while those for the other rotations are from EUVI A. Right: corresponding open field regions derived from a PFSS extrapolation of the averaged MWO/WSO photospheric field. Symbols and color-coding as in Figure 2.

(BMR) emerged at latitude $L = +33^\circ$ on 2008 November 11, with the hole forming at its western edge, within the negative-polarity sector. In this case, a counterpart positive-polarity hole does not appear at the eastern edge of the active region; instead, some of the negative-polarity open flux from the nearby polar hole closes down by connecting to the trailing (positive-polarity) sector of the active region. As pointed out by Sheeley et al. (1989; see also Benevolenskaya et al. 2001), this footpoint exchange or "interchange reconnection" process gives rise to a band of enhanced emission along the polar hole boundary, marking the footpoints of the previously open field lines. Meanwhile, as seen from Figure 4, the small mid-latitude hole soon evolves into an extension of the north polar hole, which subsequently becomes strongly sheared and decays away after only ~two rotations, in contrast to the long-lived equatorial holes described in Section 2. Given its relatively high latitudinal location, it is not surprising that this new-cycle hole gives rise to only a very weak wind stream in the ecliptic during CR 2077–2079, with peak speeds of ~400 km $\mathrm{s}^{-1}$ (the in situ data are not reproduced here). This slow wind originates from the rapidly diverging flux tubes rooted along the equatorward edge of the hole.

The emergence of the bipole in this example was accompanied by only a small change in the Sun's net dipole strength and total open flux. Correspondingly, the new hole was formed mainly through interchange reconnection with the north polar hole at the X-point of the intervening pseudostreamer, rather than through the opening-up of flux at the cusp of a helmet streamer.

The evolution of this mid-latitude hole can be simulated using a flux transport model. Adopting as the initial flux distribution the averaged MWO/WSO map for CR 2076, we determine the photospheric field $B_r(R_\odot, L, \phi, t)$ at subsequent times $t$ by numerically integrating the equation

$$\frac{\partial B_r}{\partial t} = -\Omega(L)\frac{\partial B_r}{\partial \phi} + \kappa\nabla_\perp^2 B_r - \frac{1}{R_\odot \cos L}\frac{\partial}{\partial L}\left[v(L)B_r \cos L\right]. \tag{1}$$

Here $\nabla_\perp^2$ represents the $L$ and $\phi$ components of the Laplacian, $\Omega(L) = 13.38 - 2.30\sin^2 L - 1.62\sin^4 L$ deg $\mathrm{day}^{-1}$ is the synodic rotation rate of the photospheric plasma (as inferred from magnetic tracers by Snodgrass 1983), $\kappa$ is the diffusion coefficient associated with the nonstationary supergranular convection (Leighton 1964), and $v(L)$ is the meridional flow velocity, directed poleward in each hemisphere. As in Wang et al. (2009b), we take $\kappa = 500$ $\mathrm{km^2\ s^{-1}}$ and set

$$v(L) = \pm v_m \sin^{0.1}|L|\cos^{1.8}L, \tag{2}$$

with $v_m = 17$ m $\mathrm{s}^{-1}$, which reproduces the observed variation of the polar fields during cycle 23.

Figure 5 shows how the distribution of open field regions evolves as the photospheric field is transported over four 27.3 day rotations; in order to include the effect of new flux emergence, the simulations for CR 2079–2080 were initialized

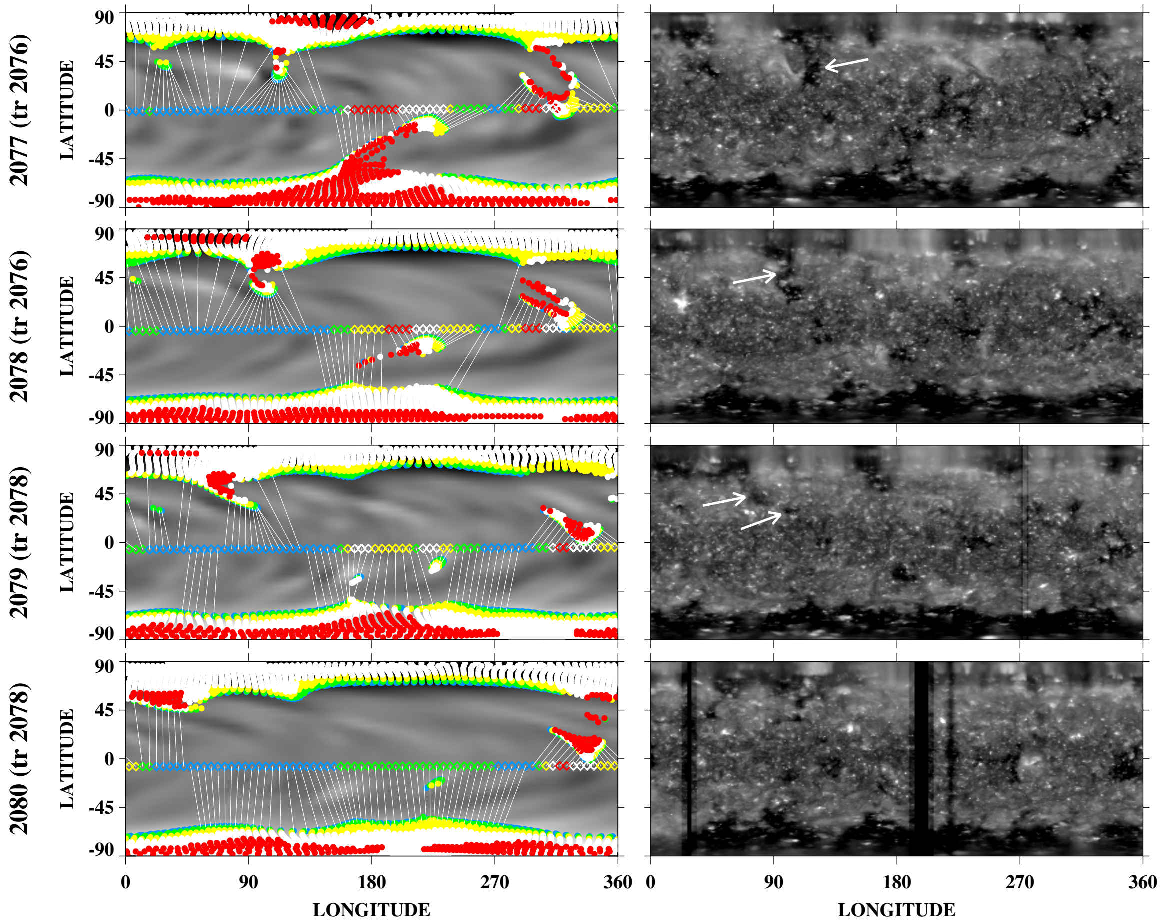


**Figure 5.** Evolution of the mid-latitude coronal hole in Figure 4, as simulated using the photospheric flux-transport model with differential rotation, supergranular diffusion at a rate of 500 km$^2$ s$^{-1}$, and a poleward bulk flow of amplitude 17 m s$^{-1}$. Left: open field regions derived for CR 2077–2080 by applying a PFSS extrapolation to the simulated photospheric field (plotted underneath). The calculations for CR 2077–2078 (CR 2079–2080) were initialized using the averaged MWO/WSO photospheric field for CR 2076 (CR 2078). Symbols, gray scale, and color-coding as in Figure 2. Right: corresponding Fe XII 19.5 nm maps constructed from EUVI A images, with white arrows indicating the observed mid-latitude hole.

using the MWO/WSO photospheric map for CR 2078. The formation of the polar hole extension at $\phi \sim 115°$ and its subsequent shearing are evidently well reproduced by the model. The rapid decay of this coronal hole is due to the steepness of the rotational gradients at midlatitudes; the "stirring" effect of the strong photospheric differential rotation accelerates the diffusive annihilation of the large-scale nonaxisymmetric field. The mid-latitude extension drifts backward in the Carrington frame because its active-region source rotates with a period of order 28.7 days.

Figure 5 also shows the final dissolution of the large south polar-hole extension that formed ~20 rotations earlier (Figure 2). The longevity of this structure can be attributed both to new injections of flux at an "active longitude" and to the fact that these old-cycle active regions were located near the equator, where the rotational shearing is at its minimum. In the absence of further activity, an equatorial hole decays on the timescale $\tau_{\rm flow} \sim R_\odot/v_m \sim 1.3$ yr (17 m s$^{-1}/v_m$) for meridional flow to carry the nonaxisymmetric flux to midlatitudes, where it is then annihilated by differential rotation and diffusion.

## 4. FORMATION OF OPPOSITE-POLARITY HOLES AROUND A NEW-CYCLE ACTIVITY COMPLEX

In the sequence of EUVI A 19.5 nm maps in Figure 6, two new-cycle BMRs emerge alongside each other near $L = +20°$ in 2009 May (CR 2083), and a small negative-polarity hole forms at the western edge of the activity complex. As illustrated by the coronal field-line plots in Figure 7, open flux is transferred via interchange reconnection from the boundary of the north polar hole to the negative-polarity sector of the westernmost active region. The transfer gives rise to a pseudostreamer overlying the interposed band of positive-polarity flux. During subsequent rotations, the small open field region evolves into an extension of the north polar hole and becomes progressively sheared, as in the previous example. In addition, however, a counterpart positive-polarity hole appears on the southeastern side of the complex. This hole, which has the "wrong" polarity for its hemisphere, closes down again during CR 2086.

Figure 8 illustrates the day-to-day evolution of the small negative-polarity hole during 2009 June 2–7, as observed from EUVI B in Fe XII 19.5 nm. The hole undergoes continual changes in shape, as adjacent fragments darken and dissolve again into the diffuse background or merge into a larger structure. On June 3, a filament eruption near the north pole acts to close down the hole(s), with the negative-polarity open flux being transferred back to the boundary of the north polar hole via interchange reconnection at the cusp of the intervening pseudostreamer. Subsequently, on June 5, the holes reappear at slightly different locations, and the fragments eventually coalesce on June 7. From this example, it is readily understood why the slow wind from small active-region holes should

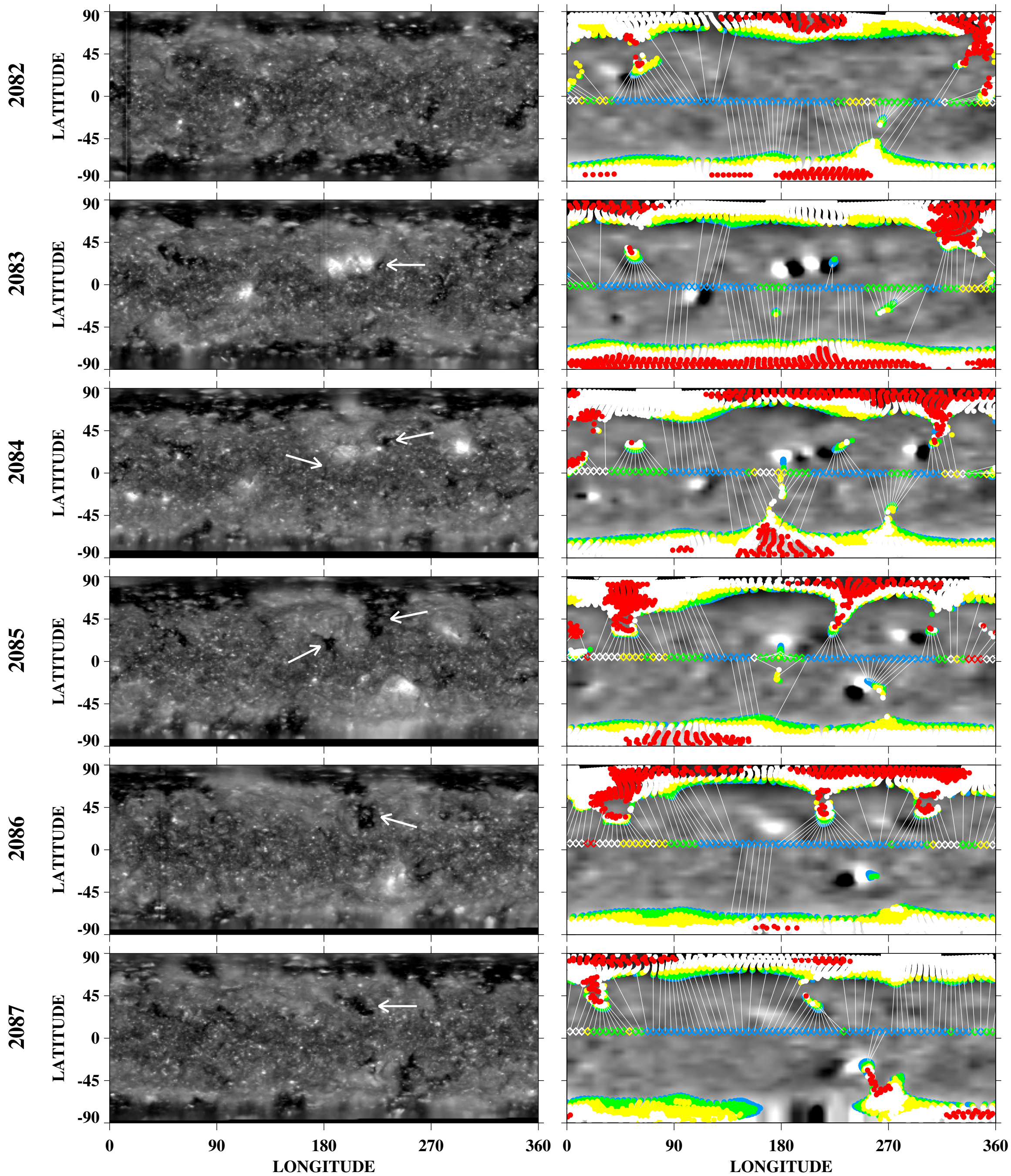


**Figure 6.** Formation of a pair of opposite-polarity holes following the emergence of two new-cycle BMRs at latitude $L \sim +20^\circ$ in 2009 May. Left: sequence of Fe xii 19.5 nm maps for CR 2082–2087 (2009 April 5 through September 16), constructed from the central meridian portions of full-disk EUVI A images. White arrows point to the evolving coronal holes. Right: corresponding open field regions derived from a PFSS extrapolation of the averaged MWO and WSO photospheric field maps for each rotation. Symbols, gray scale, and color-coding as in Figure 2.

exhibit so much temporal variability. In addition to transient disruptions by nearby coronal mass ejection (CME) events, two major factors contributing to the short-term fluctuations in coronal hole boundaries are the local emergence of ephemeral regions (as illustrated by the June 2–3 frames of Figure 8) and the nonsteady supergranular convection, which continually rearranges the network distribution of the photospheric flux, as new cells form and decay on a timescale of 1–2 days.

As shown in Figure 9, the *long-term* evolution of this coronal hole system is well reproduced by the flux transport and the PFSS models. Here, the simulation for CR 2084 was initialized using the MWO/WSO photospheric map for CR 2083, while the simulations for CR 2085–2088 were initialized using the MWO/WSO photospheric map for CR 2084. The negative-polarity extension becomes detached from the north polar hole as a swath of positive-polarity flux, originating from a decaying BMR that emerged during CR 2084, slices into it from the west. By CR 2088, the greatly sheared hole has decayed away.

In the present example, the emergence of the small new-cycle complex during CR 2083 led to a slight decrease in the Sun's net dipole strength and total open flux, because the axial (north–south) dipole moments of the BMRs were oppositely directed to that of the polar fields. In general, we would expect interchange reconnection and the closing-down

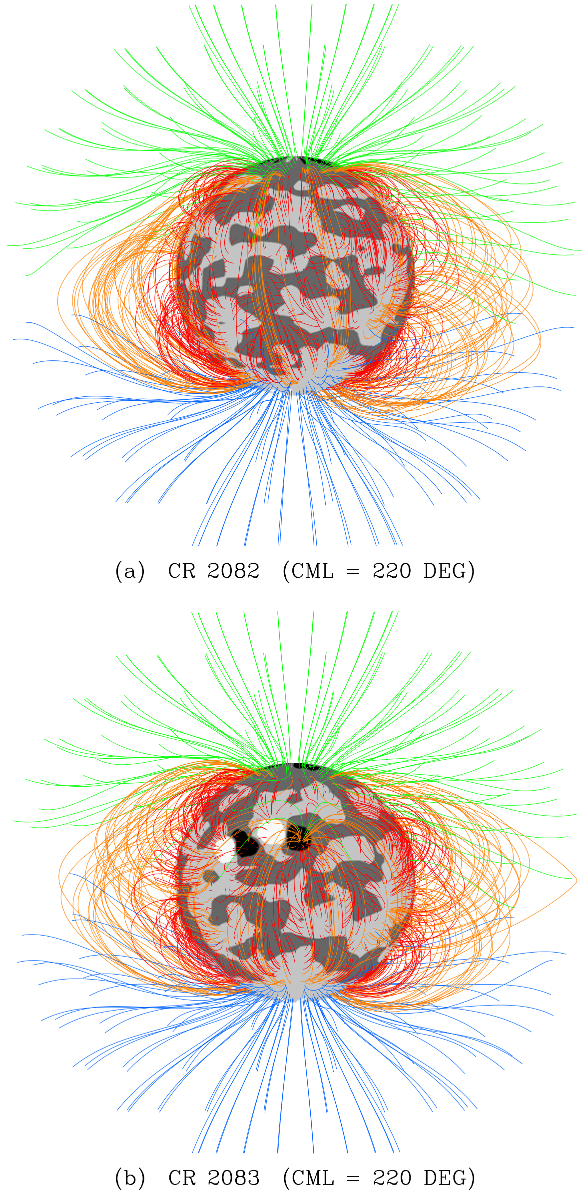


**Figure 7.** Coronal field-line topology for (a) CR 2082 and (b) CR 2083, derived from a PFSS extrapolation of the MWO/WSO photospheric field. Central meridian is at $\phi = 220^\circ$ in both cases (compare Figure 6, top two rows). Closed loops are coded orange if they extend beyond $r = 1.5\ R_\odot$, red otherwise; open field lines are blue (green) if they have positive (negative) polarity. Black, dark gray, light gray, and white denote areas of the photosphere where the radial field component lies in the ranges $B_r < -6$ G, $-6$ G $< B_r < 0$ G, $0$ G $< B_r < +6$ G, and $B_r > +6$ G, respectively. The emergence of the pair of mid-latitude bipoles causes open flux to be transferred from the north polar hole to the negative-polarity sector of the westernmost bipole, forming the small coronal hole seen in the 19.5 nm map for CR 2083 in Figure 6.

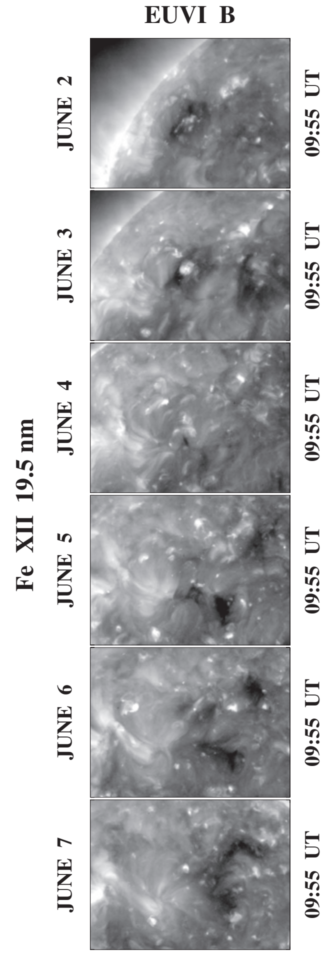


**Figure 8.** Day-to-day evolution of the small negative-polarity hole in Figure 6, as observed with EUVI B during 2009 June 2–7. All of the Fe XII 19.5 nm images were recorded at 09:55:30 UT. The near-disappearance of the hole on June 4 coincided with a filament eruption near the north pole. Despite the large short-term fluctuations, the general tendency is for the hole to increase in size through the coalescence of separate fragments.

of flux to dominate over the opening-up of flux during the rising phase of the cycle, up to the time of polar field reversal (see Figure 6 in Wang & Sheeley 2003b).

Figure 10 shows the wind speeds, proton densities, and spiral angles recorded at *ACE* during CR 2083–2087. The wind streams generated by the emergence of the new-cycle active regions are marked by vertical dashes. The stream associated with the north polar-hole extension persists for three rotations (CR 2085–2087); the maximum speeds are less than $\sim$500 km s$^{-1}$ because only the rapidly diverging flux tubes rooted just inside the hole boundary reach down into the ecliptic plane. The stream from the short-lived, positive-polarity hole is observed only during CR 2085 (with possibly a very weak remnant present during CR 2086). The density spike appearing near $\phi = 90^\circ$ during CR 2083–2085 may represent a pseudostreamer plasma sheet. This feature is located at the interface between the wind stream from a small mid-latitude hole and the slow wind from the boundary of the north polar hole.

## 5. SUMMARY AND DISCUSSION

Taking advantage of the prolonged period of low activity at the end of cycle 23, we have been able to track individual coronal holes over several rotations following their birth in active regions and to demonstrate the essential role of photospheric flux transport in their evolution. It should be emphasized that these transport processes (supergranular convection, differential rotation, and meridional flow) act on the entire photospheric field without regard to whether the flux is open or closed; the coronal field-line configuration then rearranges itself in response to global changes in the photospheric flux distribution, so as to remain close to a current-free state (the photospheric "dog" wags the coronal "tail," not the other way around). In summary, the distribution of coronal holes and their evolution are determined by three principal factors: (1) the emergence of active regions, whose outermost loops expand outward and open up, or undergo interchange reconnection with preexisting

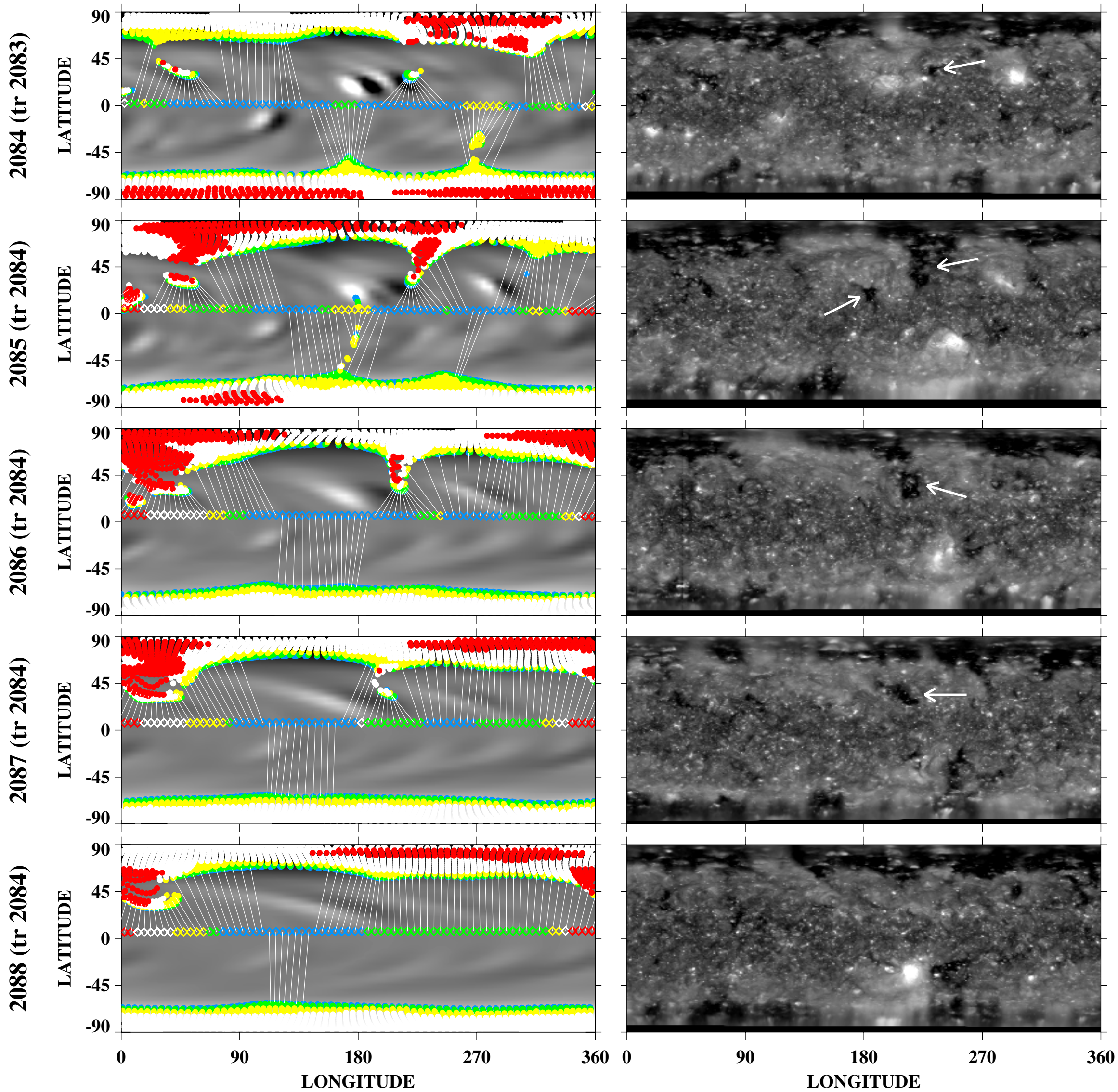


**Figure 9.** Flux-transport simulation of the polar-hole extension in Figure 6. Left: open field regions derived for CR 2084–2088 by applying a PFSS extrapolation to the simulated photospheric field (plotted underneath). The calculations for CR 2084 (CR 2085–2088) were initialized using the averaged MWO/WSO photospheric map for CR 2083 (CR 2084). Symbols, grayscale, and color-coding as in Figure 2. Right: corresponding Fe xii 19.5 nm maps constructed from EUVI A (CR 2084–2087) and EUVI B (CR 2088) images.

open flux, to form small coronal holes; (2) the redistribution of the active-region flux via photospheric transport processes, which give rise to the large unipolar regions where the holes grow to their maximum size and which eventually lead to the annihilation of the nonaxisymmetric component of the open flux at midlatitudes; and (3) field-line reconnection, which takes place at the cusps of helmet streamers and pseudostreamers and allows the coronal field to relax toward a potential state (see Nash et al. 1988; Wang & Sheeley 1993, 2004; Fisk & Schwadron 2001; Crooker et al. 2002; Lionello et al. 2005).

On timescales of a day and less, the hole boundaries and the small active-region holes themselves undergo continual fluctuations on spatial scales comparable to that of the supergranular network (see Figure 8). These fluctuations, which may be associated both with footpoint exchanges with closed loops and with the actual transport of open flux by photospheric motions, are likely to be a major contributor to the variability of the slow solar wind.

Although the PFSS method is remarkably successful at predicting the locations of coronal holes, it does not tell us how the active-region loops are converted into open flux, but simply assumes that all field lines that extend beyond $r = R_{ss} \sim 2.5\ R_{\odot}$ are dragged out into the heliosphere. An important question concerns the relationship between CME events and the formation of long-lived coronal holes (Luhmann et al. 1998; Owens & Crooker 2006). While it has long been known that CMEs and slow streamer blowouts give rise to transient holes and coronal dimming regions, a direct association between CMEs and coronal holes that persist for more than $\sim$1 rotation has yet to be established. Instead, the holes tracked here appeared to form over timescales comparable to or greater than that for the active regions to emerge, developing stealthily from small, low-contrast regions at the peripheries or from barely visible dark lanes. The gradual opening-up of active-region loops to form a quasisteady wind and small coronal hole could be simulated by including the effects of coronal heating,

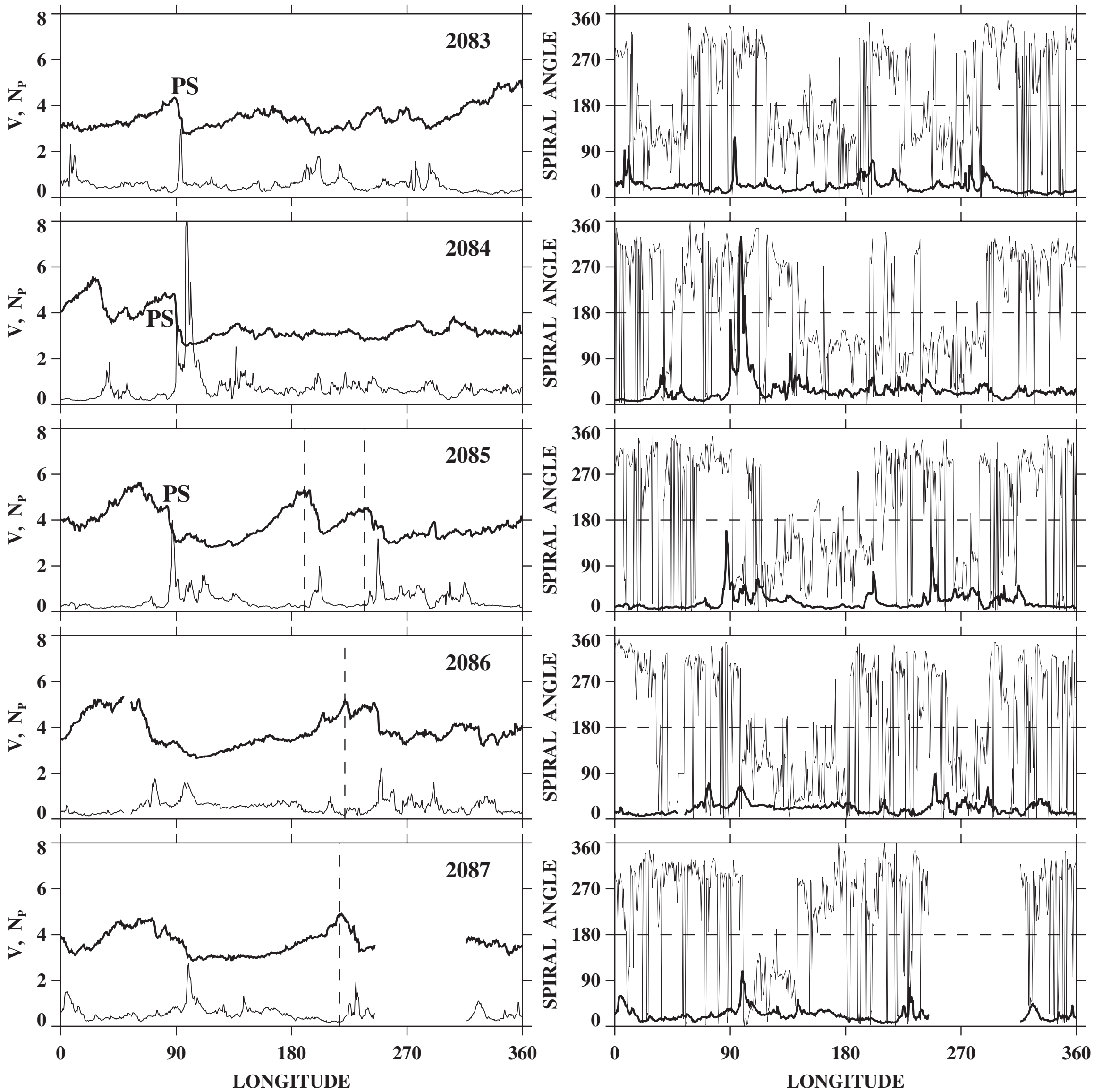

**Figure 10.** Solar wind measurements by *ACE* during CR 2083–2087, plotted as a function of Carrington longitude. As in Figure 3, the data have been mapped back to the source surface by assuming a five-day Sun–Earth travel time. Left: hourly averages of the wind speed $v$ in units of 100 km s$^{-1}$ (thick solid line) and the proton density $n_p$ in units of 10 cm$^{-3}$ (thin solid line). Vertical dashes mark the wind streams generated by the arrowed coronal holes in Figure 6. A plasma sheet that may be associated with a pseudostreamer is also identified near $\phi = 90°$ during CR 2083–2085. Right: variation of the spiral angle in degrees (thin solid line) and proton density in arbitrary units (thick solid line).

downward heat conduction, and radiative losses in MHD models of emerging BMRs.

The relative paucity of CME events during 2007–2009 and the presence of so many low- and mid-latitude holes (which in turn is related to the weakness of the polar fields) have allowed us to identify a number of plasma sheets that may be the in situ counterparts of coronal pseudostreamers. These narrow density spikes, typically only a few hours wide, occur at the interface between wind streams of the same polarity (see also Neugebauer et al. 2002). While the compressive interaction between the tail end of the leading stream and the front end of the trailing stream will further steepen the density profile, coronagraph images show that high-density sheets are already present in the outer corona along the boundaries between like-polarity coronal holes. These structures tend to be somewhat fainter than the plasma sheets located at polarity reversals because the surrounding field diverges more rapidly with heliocentric distance (whereas the field lines above a helmet streamer cusp are "refocused" by the current sheet, resulting in a falloff less steep than $r^{-2}$).

Figure 3 shows that the Fe/O ratio is sometimes sharply peaked at plasma sheets, whether or not they are located at polarity reversals. Borrini et al. (1981) found that the He/H ratio dips sharply at plasma sheets associated with sector boundaries. One interpretation of these results is that the source of the plasma sheet material differs from that of the bulk of the slow wind, with the former being ejected from the closed portions of helmet streamers and pseudostreamers, and the latter originating from rapidly diverging, open flux tubes rooted just inside the coronal hole boundaries. Suess et al. (2009) have suggested that the sharp dip in He/H that Borrini et al. (1981) observed at sector-boundary plasma sheets is an artifact of their superposed-epoch analysis, and that the actual minimum is much broader. Indeed, not all of the Fe/O enhancements seen in the left-hand panels of Figure 3 coincide with plasma sheets, and it may be that transient releases of closed-field material may propagate into the open flux domain containing the bulk of the slow wind.

Finally, we note that the EUV Imaging Spectrometer on *Hinode* has detected outward flows of ∼10 km $s^{-1}$ and greater (ranging up to 200 km $s^{-1}$) in active regions, including the activity complex in Figure 2 (Doschek et al. 2008; Harra et al. 2008; Sakao et al. 2007; Bryans et al. 2010). The flows are concentrated in areas of relatively weak Fe XII 19.5 nm emission. However, because these areas appear to lie well outside the boundaries of the coronal holes themselves, the Doppler velocity maps may be showing transient flows along long closed loops, rather than the actual escape of material along open field lines to form the solar wind.

We are indebted to R. K. Ulrich (MWO) and J. T. Hoeksema (WSO) for making the photospheric field data used in this paper available. We also thank N. U. Crooker and M. Neugebauer for helpful discussions on the in situ signatures of coronal pseudostreamers. This work was supported by NASA and the Office of Naval Research.

## REFERENCES

Abramenko, V., Yurchyshyn, V., Linker, J., Mikić, Z., Luhmann, J., & Lee, C. O. 2010, ApJ, 712, 813
Arge, C. N., Hildner, E., Pizzo, V. J., & Harvey, J. W. 2002, J. Geophys. Res., 107, 1319
Arge, C. N., & Pizzo, V. J. 2000, J. Geophys. Res., 105, 10465
Benevolenskaya, E. E., Kosovichev, A. G., & Scherrer, P. H. 2001, ApJ, 554, L107
Borrini, G., Gosling, J. T., Bame, S. J., Feldman, W. C., & Wilcox, J. M. 1981, J. Geophys. Res., 86, 4565
Bryans, P., Young, P. R., & Doschek, G. A. 2010, ApJ, in press
Chen, Y., Li, X., Song, H. Q., Shi, Q. Q., Feng, S. W., & Xia, L. D. 2009, ApJ, 691, 1936
Cranmer, S. R. 2009, Living Rev. Solar Phys., 6, 3
Crooker, N. U., Gosling, J. T., & Kahler, S. W. 2002, J. Geophys. Res., 107, 1028
Crooker, N. U., Huang, C.-L., Lamassa, S. M., Larson, D. E., Kahler, S. W., & Spence, H. E. 2004, J. Geophys. Res., 109, A03107
Doschek, G. A., Warren, H. P., Mariska, J. T., Muglach, K., Culhane, J. L., Hara, H., & Watanabe, T. 2008, ApJ, 686, 1362
Fisk, L. A., & Schwadron, N. A. 2001, ApJ, 560, 425
Geiss, J., et al. 1995, Science, 268, 1033
Gibson, S. E., Kozyra, J. U., de Toma, G., Emery, B. A., Onsager, T., & Thompson, B. J. 2009, J. Geophys. Res., 114, A09105
Gloeckler, G., et al. 1998, Space Sci. Rev., 86, 497
Harra, L. K., et al. 2008, ApJ, 676, L147
Harvey, K. L., & Hudson, H. S. 2000, Adv. Space Res., 25, 1735
Howard, R. A., et al. 2008, Space Sci. Rev., 136, 67
Lee, C. O., et al. 2009, Sol. Phys., 256, 345
Leighton, R. B. 1964, ApJ, 140, 1547
Levine, R. H., Altschuler, M. D., & Harvey, J. W. 1977, J. Geophys. Res., 82, 1061
Liewer, P. C., Neugebauer, M., & Zurbuchen, T. 2004, Sol. Phys., 223, 209
Lionello, R., Riley, P., Linker, J. A., & Mikić, Z. 2005, ApJ, 625, 463
Luhmann, J. G., Gosling, J. T., Hoeksema, J. T., & Zhao, X. 1998, J. Geophys. Res., 103, 6585
Luhmann, J. G., et al. 2009, Sol. Phys., 256, 285
McComas, D. J., Bame, S. J., Barker, P., Feldman, W. C., Phillips, J. L., Riley, P., & Griffee, J. W. 1998, Space Sci. Rev., 86, 563
McComas, D. J., et al. 2007, Rev. Geophys., 45, RG1004
Nash, A. G., Sheeley, N. R., Jr., & Wang, Y.-M. 1988, Sol. Phys., 117, 359
Neugebauer, M., Liewer, P. C., Smith, E. J., Skoug, R. M., & Zurbuchen, T. H. 2002, J. Geophys. Res., 107, 1488
Owens, M. J., & Crooker, N. U. 2006, J. Geophys. Res., 111, A10104
Rosenberg, R. L., & Coleman, P. J., Jr. 1969, J. Geophys. Res., 74, 5611
Rouillard, A. P., et al. 2009, Sol. Phys., 256, 307
Sakao, T., et al. 2007, Science, 318, 1585
Schrijver, C. J., & DeRosa, M. L. 2003, Sol. Phys., 212, 165
Sheeley, N. R., Jr., Lee, D. D.-H., Casto, K. P., Wang, Y.-M., & Rich, N. B. 2009, ApJ, 694, 1471
Sheeley, N. R., Jr., Wang, Y.-M., & Harvey, J. W. 1989, Sol. Phys., 119, 323
Smith, C. W., L'Heureux, J., Ness, N. F., Acuña, M. H., Burlaga, L. F., & Scheifele, J. 1998, Space Sci. Rev., 86, 613
Snodgrass, H. B. 1983, ApJ, 270, 288
Song, H. Q., Chen, Y., Liu, K., Feng, S. W., & Xia, L. D. 2009, Sol. Phys., 258, 129
Suess, S. T., Ko, Y.-K., von Steiger, R., & Moore, R. L. 2009, J. Geophys. Res., 114, A04103
Švestka, Z., Solodyna, C. V., Howard, R., & Levine, R. H. 1977, Sol. Phys., 55, 359
Ulrich, R. K., Bertello, L., Boyden, J. E., & Webster, L. 2009, Sol. Phys., 255, 53
Ulrich, R. K., Evans, S., Boyden, J. E., & Webster, L. 2002, ApJS, 139, 259
von Steiger, R., et al. 2000, J. Geophys. Res., 105, 27217
Wang, Y.-M. 2009, Space Sci. Rev., 144, 383
Wang, Y.-M., Ko, Y.-K., & Grappin, R. 2009a, ApJ, 691, 760
Wang, Y.-M., Robbrecht, E., & Sheeley, N. R., Jr. 2009b, ApJ, 707, 1372
Wang, Y.-M., & Sheeley, N. R., Jr. 1990, ApJ, 355, 726
Wang, Y.-M., & Sheeley, N. R., Jr. 1993, ApJ, 414, 916
Wang, Y.-M., & Sheeley, N. R., Jr. 1995, ApJ, 447, L143
Wang, Y.-M., & Sheeley, N. R., Jr. 2003a, ApJ, 590, 1111
Wang, Y.-M., & Sheeley, N. R., Jr. 2003b, ApJ, 599, 1404
Wang, Y.-M., & Sheeley, N. R., Jr. 2004, ApJ, 612, 1196
Wang, Y.-M., Sheeley, N. R., Jr., & Rich, N. B. 2007, ApJ, 658, 1340
Wang, Y.-M., et al. 1998, ApJ, 498, L165
Zurbuchen, T. H. 2007, ARA&A, 45, 297